Origin of natural and magnetic field induced polar order in orthorhombic PrFe$_{1/2}$Cr$_{1/2}$O$_3$

Anil Kumar ®,[1,*] M. Kamal Warshi ®,[1] Archna Sagdeo ®,[2,3] Matthew Krzystyniak ®,[4] Svemir Rudić,[4] D. T. Adroja ®,[4] Ivan da Silva ®,[4] and P. R. Sagdeo ®[1,†]

[1]*Material Research Laboratory, Department of Physics, Indian Institute of Technology, Indore 453552, India*
[2]*Synchrotron Utilization Section, Raja Ramanna Center for Advanced Technology, Indore 452013, India*
[3]*Homi Bhabha National Institute, Training School Complex, Anushakti Nagar, Mumbai 400094, India*
[4]*ISIS Facility, STFC Rutherford Appleton Laboratory, Chilton, Didcot, Oxfordshire OX11 0QX, United Kingdom*

Here, we report the possible origin of natural and magnetic field induced polar order near room temperature (RT) in PrFe$_{1/2}$Cr$_{1/2}$O$_3$. The temperature-dependent Raman spectroscopy (RS) and synchrotron x-ray diffraction experiments disregard any change in the structure at low temperatures, which is not compatible with the emergence of natural ferroelectricity in this sample. Further, inelastic neutron scattering, neutron Compton scattering, neutron resonance transmission analysis and magnetic field-dependent RS experiments, suggest an increase in the delocalization of Pr^{3+} ions in PrFe$_{1/2}$Cr$_{1/2}$O$_3$ with respect to the parent compound PrFeO$_3$. The evaluation of the present results reveals that more delocalized Pr^{3+} ions and strong spin-phonon coupling in PrFe$_{1/2}$Cr$_{1/2}$O$_3$ seem to be a driving force for the observed natural and magnetic field induced switchable polar order in PrFe$_{1/2}$Cr$_{1/2}$O$_3$. The present results provide a significant contribution in understanding the ferroelectric polarization and progress in the search for RT magnetodielectric materials.

I. INTRODUCTION

In recent times, magnetodielectric materials have gained huge attention from the research community by virtue of various interesting fundamental properties and possible applications [1,2]. The mutual coupling between magnetic (electric) and ferroelectric (magnetization) orders offer an opportunity to write down the magnetic information with the application of a very small electric field [1,3,4]. Hence, maximizing the mentioned coupling between electric and magnetic parameters has great importance in technological applications [5]. However, there are only a limited number of materials present which possess strong magneto-electric coupling near room temperature (RT) to be useful for practical applications [5]. Thus, searching for materials that exhibit such a coupling has become the need of the day, which increases the possibility of designing RT-based devices [5]. The development of silicon-based tiny integrated circuits has opened an avenue for research in the direction of exploring materials for various electronic applications [6,7]. Nowadays, research is focused on developing tiny as well as energy-efficient electronic devices and replacing the conventional electronic circuit elements. The efforts are now being made to develop spin-based electronic devices, and in these directions, perovskite oxides are of great interest [4,6–9]. Among these perovskite oxides, rare earth orthochromites (RCrO$_3$, R = rare earth atom) and orthoferrites (RFeO$_3$) have been investigated for several decades due to their remarkable potential applications as well

as underlying physics [10–13]. These perovskite oxides have been proposed for various applications in spintronics devices [14], chemical sensors [15], magneto-electric devices [3,5], as well as ultrafast magneto-optical storage devices [16,17]. The importance of these materials now enormously exceeds the applications predicted at the start of the multiferroics rebirth at the turn of this century.

Over the following decades, there has been an excessive increase in understanding the fundamental physics of ferroelectrics, which in turn has significantly contributed to optimizing materials for device applications [5,8,18]. There are several centrosymmetric materials which exhibit natural polar order because of a certain type of magnetic ordering [13,19]. Among various centrosymmetric materials, the orthorhombic maganites have been thoroughly investigated in which ferroelectricity appears due to cycloidal spin structure appearing at magnetic ordering temperature [20,21]. Recently, orthochromites with magnetic rare earth ions have been explored from this perspective, and it is reported that ferroelectricity below Néel's temperature (T_{N1}) is attributed to the magnetic interactions between Cr and rare earth ions, and the similar mechanism is known to be responsible for the ferroelectricity in rare earth orthoferrites [22]. Recently, in SmFeO$_3$, ferroelectric features have been reported $< T_{N1}$ (670 K) [23], which is completely surprising, as it would require R ion moments to order at very low temperature (<15 K). Therefore, the exchange striction mechanism cannot solely explain the cause of polarization observed at high temperatures. Also, according to the inverse Dzyaloshinskii-Moriya interaction model for canted antiferromagnetic systems, there is zero net polarization because of cancellation of local polarization resulting from alter-

---
*Corresponding author: garry.anil1369@gmail.com
†prs@iiti.ac.in

nate arrangement of pairs of canted spins [24,25]. It can be mentioned here that R and Fe^{3+} ions exhibit anisotropic interactions, and it may induce net dipole moments in these oxides. More importantly, recent research on $SmFeO_3$ samples revealed that there exists spontaneous electric polarization at 173 K [25]. Bhadram *et al.* [10] reported that the spin-phonon coupling (SPC) plays an important role in stabilizing the polar order in RFe/CrO_3 oxides. First-principles calculations carried out on these systems suggested that there might be occurrence of electric polarization along the b axis, where the exchange striction mechanism is attributed to the polar displacement of the oxygen ions associated with the proposed ferroelectricity [26] Of particular interest is the possibility of having magnetically driven improper ferroelectricity [27,28], as in the much-studied families of rare earth orthochromites and orthoferrites, yet the mechanisms behind such effects remain to be understood in detail. The observation of such contradictory results gives rise to arguments to the occurrence of intrinsic ferroelectricity in these systems. Therefore, there has been an intense debate on the exact origin of ferroelectric order in these oxides. Hence, the probing of local structure is very important to understand the observed class of ferroelectricity in these materials.

In this paper, we focus on the $PrFe_{1/2}Cr_{1/2}O_3$ ceramic and its end members, i.e., $PrFeO_3$ and $PrCrO_3$, which crystallize in orthorhombic structure with space group $Pnma$ [10,22,29], Significant efforts have been made by various research groups to understand the multiferroic properties of these compounds [19,25,29–31]; however, the origin of the natural and magnetic field induced polar order in these samples is still not clear. Further, it is worth noting that the magnetic ordering temperature in these orthoferrite oxides can be tuned to RT with doping, and the strength of magneto-dielectric coupling is maximum around transition temperature [1,4]. The magnetic ordering temperature (T_{N1}) for the parent $PrFeO_3$ sample is 700 K, and for $PrFe_{1/2}Cr_{1/2}O_3$, T_{N1} is near RT [32]. Therefore, it could be possible to tune the orientations of spins by applying a very small magnetic field by means of magnetostriction. Thus, inclusion of Cr^{3+} ions at Fe^{3+} sites in orthoferrites would scale the possibility of magnetodielectric coupling for designing RT-based devices [5,32]. Further, the ever-increasing demand of high-performance and multitasking micro-electronic devices that can store and share information in an easier and faster way has motivated scientists to search for materials with multifunctional properties for reading, writing, and data sharing processes [6,28]. Up to now, $BiFeO_3$ and related systems are the only known compounds which simultaneously possess such characteristics. In this paper, we show that another family of materials, namely, mixed Fe-Cr-based rare earth materials ($PrFe_{1/2}Cr_{1/2}O_3$), can also exhibit such desired features.

Herein, we report the origin of natural and magnetic field induced polar order $<T_{N1}$, and it has been reported that the anomalies in the low-frequency modes related to Pr ion motion and the presence of SPC support the suggestion that the coupling between $4f$-$3d$ moments play an important role in inducing switchable electric polarization. The derived data demonstrate an increased magnitude of delocalization of Pr^{3+} ions in the presence of Cr in the lattice at RT, which seems to be one of the important contributing factors for the observed

ferroelectric behavior in $PrFe_{1/2}Cr_{1/2}O_3$. Further, inelastic neutron scattering (INS), neutron Compton scattering (NCS), neutron resonance transmission analysis (NRTA), and magnetic field-dependent Raman spectroscopy (RS) experiments support an increase in the delocalization of Pr^{3+} ions in $PrFe_{1/2}Cr_{1/2}O_3$ with respect to the parent sample $PrFeO_3$.

II. EXPERIMENTAL DETAILS

A. Sample preparation by Sol-Gel method

The $PrFeO_3$ and $PrFe_{1/2}Cr_{1/2}O_3$ samples were synthesized by the wet chemical method [33,34]. The synthesis process involved the formation of an aqueous solution of precursors by dissolving praseodymium nitrate hexahydrate $Pr(NO_3)_3.6H_2O$ (99.99%, Sigma Aldrich), iron nitrate [$Fe(NO_3)_3.9H_2O$ (99.99%, Sigma Aldrich)], and chromium nitrate [$Cr(NO_3)_3.9H_2O$ (99.99%, Sigma Aldrich)]. The resulting solution was mixed in an equimolar mixture of citric acid and ethylene glycol under continuous stirring and heating at 70 °C until a gel is formed, and the prepared gel was heated in a muffle furnace for 12 h at 1200 °C.

B. Sample characterization techniques

1. Structural characterization

The structural phase purity of the prepared sample was confirmed by performing synchrotron x-ray diffraction (SXRD) at Indus-2 Indian Synchrotron Radiation Source at Beamline BL-12 using a Huber 5020 diffractometer. The beam energy used for the measurements was 15 keV. The x-ray wavelength used in this paper was 0.756 Å and was precisely calibrated by measuring the XRD pattern of the NIST LaB_6 standard sample. The SXRD data have been refined by considering the space group $Pnma$ [12]. The one-to-one comparison of experimental data with the fitted data clearly suggests the phase purity of the prepared sample.

2. Magnetic measurements

To understand the magnetic ordering temperature and spin reorientation (SR) temperature in $PrFe_{1/2}Cr_{1/2}O_3$, temperature-dependent (TD) direct current magnetization measurements were carried out using the magnetic property measurement system (MPMS, Quantum Design, USA) in 500 Oe magnetic field and temperature ranging from 5 to 310 K [35].

3. TD Raman experiments

The TD vibrational properties of the prepared samples were investigated by using a LABRAM HR dispersive spectrometer equipped with a 633 nm excitation laser source with a grating of 1800 grooves/mm [35–39]. Further, a 50× magnification glass-compensating objective was used, and the beam power was kept <1 mW outside the cryostat to reduce the local heating in the illuminated spot. However, during this study, several different settings, integration times, and power densities were used with no significant change in the general appearance of the data. The TD Raman measurements were carried out using the THMS600 stage from Linkam, having an accuracy of the order of 0.1 K [12]. The block diagram

of the major components of the Raman spectrometer setup is depicted in Fig. S01 (see Supplemental Material [40]).

4. Inelastic, deep inelastic (Compton) neutron scattering and NRTA

NCS and NRTA measurements were performed at VESU-VIO [41–44], whereas INS experiments were done at TOSCA [45–50], both inverted geometry spectrometers located at the ISIS Neutron and Muon Spallation Source at the STFC Rutherford Appleton Laboratory in Harwell, Oxfordshire, UK. The VESUVIO measurements of the $PrFeO_3$ and $PrFe_{1/2}Cr_{1/2}O_3$ samples were carried out at $T = 300$ and 10 K, whereas the TOSCA measurements [46–48,50,51] were at $T = 10$ K. The layouts of the VESUVIO and TOSCA spectrometers installed at the ISIS Pulsed Neutron and Muon Source are depicted in Figs. S02 and S03, respectively (see Supplemental Material [40]). The powder samples were kept in flat aluminum cells. The cells were assembled out of two flat (one front and one backside) walls, each of a cross-section of $64\,cm^2$, fully exposed to the incident VESUVIO neutron beam when placed perpendicular to its direction. The general setup of VESUVIO was described elsewhere [41–43,50]. The isotopic mass-resolved NCS spectra were recorded in the neutron time-of-flight (TOF) domain by detectors placed at scattering angles between $130°$ and $170°$ (referred to as the backscattering regime) [41–44]. The raw NCS data were corrected for multiple scattering effects in a self-consistent manner according to the established and widely used protocol [44]. During all subsequent steps of the NCS data correction protocol, the technique of stoichiometric fixing was applied, whereby the ratios of the integral scattering intensities of peaks present in the NCS spectra recorded in the TOF domain were constrained to be equal to the ratios of the products of the total bound scattering cross-sections and the number of moles of the respective nuclei per formula unit of the compound under consideration [44]. The stoichiometric fixing technique allowed for reliable fitting of the widths of the recoil peaks present in the NCS spectra despite their partial overlapping in the signals recorded in the TOF domain.

The NRTA experiments were performed concurrently with the NCS using the same sample and container. Such a global approach has already been demonstrated to be the optimal strategy in modelling nuclear quantum effects in heavyweight atomic species, largely avoiding systematic errors in the global data analysis due to instrument calibration or temperature differences [41]. The NRTA data were acquired using the incident and transmitted beam lithium-glass monitors. The data were corrected for the background from the empty instrument and fitted with the convolution of the energy resolution and Doppler-broadened Breit-Wigner formula.

5. TD dielectric measurement

The TD dielectric experiment was performed by using a precision impedance analyzer (Wynne Kerr 65120B) with an oscillator voltage of ± 1 V [52]. To perform the dielectric measurements, the obtained powdered samples were pelletized to circular pellets at high pressure of ~ 20 ton. These pellets were sintered in air at $1200\,°C$ for 24 h and then coated with silver paint on both sides to make a parallel plate capacitor.

The general TD dielectric setup is described in Fig. S04 (see Supplemental Material [40]).

III. RESULTS AND DISCUSSION

A. TD polarization measurements

An important goal of this paper is to understand the origin of natural and magnetic field induced polar order in $PrFe_{1/2}Cr_{1/2}O_3$. To realize this in the first part, we reproduced the TD polarization data, and the same has been depicted in Fig. S05 (see Supplemental Material [40]). Visible changes can be observed <280 K in $PrFe_{1/2}Cr_{1/2}O_3$, which might be due to the presence of a net dipole moment in the sample. The observed values of polarization are very small, but similar polarization values as a function of temperature have been reported for these samples in the literature [10,13,27,30,31]. It is important here to note that the observed natural polarization may have an extrinsic origin, but keeping in view the various reports published [10,13,19,27,30,31], we presumed that the observed polarization has an intrinsic origin. Further, Muniraju [53] explained the observed polar order in terms of distortion of the R^{3+} ion due to the R-Cr exchange field. Bhadram et al. [10] reported that the presence of spin-lattice coupling plays a critical role in persuading the ferroelectric polarization. Therefore, the probing of the local structure of these compounds could be very important to understand the observed class of ferroelectricity in these materials. The SXRD experiments (see Supplemental Material [40] Fig. S06) carried out on the prepared samples are best fitted by the centrosymmetric *Pnma* space group, which is not compatible with the emergence of natural ferroelectricity in this sample, and the observed polar order cannot be explained in terms of displacement of Fe/Cr ions or a noncentrosymmetric structure as in the case of classical ferroelectric materials [37]. It is worth mentioning here that the presence of P-E hysteresis loop in these samples gives an indication of the nonzero macroscopic polarization in the sample, which therefore lacks the center of inversion [19], which is not consistent with the XRD results since the XRD measurements probe the average values of lattice parameters, which implies that the diffraction signal from a coherently scattered region from the grains and global symmetry appears to be centrosymmetric [19,22,54]. Also, the diffraction signal from a coherently scattered region from the grain, which is very close to 150 nm for $PrFe_{1/2}Cr_{1/2}O_3$, and the lattice parameters were averaged out over $\sim 350+$ unit cells, and hence, global symmetry appears to be centrosymmetric [54]. Thus, the signature of noncentrosymmetry could be absent in SXRD experiments.

It is reported in the literature that the observed polar order may have a magnetic origin [27,28]. Recently, these samples have been explored from this perspective, and it is reported that ferroelectricity below Néel's temperature (T_{N1}) is attributed to the magnetic interactions between Cr and rare earth ions, and the similar mechanism is known to be responsible for the ferroelectricity in rare earth orthoferrites [22]. Therefore, to get more insight into this phenomenon, TD magnetization measurements were performed and will be elaborated in detail in the next sections.
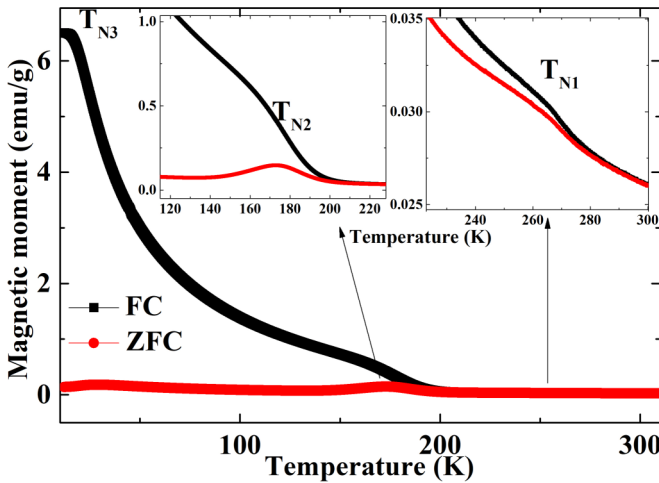
FIG. 1. Temperature dependence of the direct current magnetization variation for polycrystalline $PrFe_{1/2}Cr_{1/2}O_3$. Insets corresponding to T_{N1} and T_{N2} represent the magnetic transition and spin reorientation temperature. Low temperature ascribed as T_{N3} is due to the ordering of Pr^{3+} ions.

B. TD magnetization measurements

Figure 1 represents the TD magnetization under the field cooled and zero-field cooling mode with $H = 500$ Oe. It can be seen from the figure that $PrFe_{1/2}Cr_{1/2}O_3$ exhibits three obvious magnetic transitions at temperatures $T_{N1} = 280$ K, $T_{N2} = 160$ K, and $T_{N3} = 10$ K. The possible origin of these magnetic transitions may arise due to the presence of several magnetic interactions like Pr-O-(Fe/Cr), Pr-O-Pr, Fe-O-Cr, Cr-O-Cr, or Fe-O-Fe. It should be noted here that, in $PrCrO_3$, Pr-O-Pr and Cr-O-Cr interactions take place at <10 and 160 K, respectively, whereas in $PrFeO_3$, Fe-O-Fe and Pr-O-Pr interactions take place at 700 and <10 K, respectively [55]. The possible reasons for the increase in the magnetization values at 280 K followed by SR (160 K) will be discussed in detail.

The observed decrease in Néel temperature (T_{N1}) and increase in SR transition temperature (T_{N2}; with respect to $PrFeO_3$; $T_{N1} = 700$ K) with the inclusion of Cr^{3+} at the Fe^{3+} site is attributed to the weakening of the Fe(Cr)-O-Fe(Cr) antiferromagnetic exchange interaction. Also, we relate the changes in T_{N1} to the enhancement of ferromagnetic interaction of adjacent Cr^{3+} moments through t_{2g}-e_g hybridization due to structural distortion [29]. The weakening of Fe/Cr-O-Fe/Cr superexchange interactions with the inclusion of Cr^{3+} ions could be better described by the Goodenough-Kanamori (GK) rule [56,57] in terms of interactions between two adjacent transition metal ions with virtual charge transfer. According to the GK rule, the outermost shell electronic configuration for Cr^{3+} and Fe^{3+} are t^3e^0 and t^3e^2, respectively. In the case of orthoferrites, the σ bonding of half-filled e_g^2-O-e_g^2 orbitals and π bonding of half-filled t_{2g}^3-O-t_{2g}^3 orbitals interact through superexchange interaction and are antiferromagnetic in nature, which satisfies Hund's rule [30]. Hence, it can be concluded from here that the overlapping of these (t_{2g}-e_g) orbitals does not give rise to any extra magnetic phase component to the overall superexchange interaction.

On the contrary, in the case of orthochromates, t_{2g}-e_g hybridization gives an additional ferromagnetic component to the existing antiferromagnetic interaction. Due to the presence of antiferromagnetic and ferromagnetic interactions and interplay between them through t_{2g}-e_g hybridization, the strength of ferromagnetic interaction increases, and antiferromagnetic interaction decreases with the inclusion of Cr in $PrFeO_3$, which seems to be responsible for the decrease in T_{N1} with respect to $PrFeO_3$.

In addition to this, the observed variation in T_{N1} is consistent with the molecular field theory. According to this theory, the correlation between T_N and J is defined as [58]

$$\frac{J}{k} = \frac{3T_N}{2zS(S+1)}, \tag{1}$$

where k is Boltzmann's constant, z is the nearest neighbor's number, i.e., six for $RFeO_3$, J is the strength of superexchange interaction between nearest-neighbor ions, $S = \frac{5}{2}$ and $\frac{3}{2}$ for Fe^{3+} and Cr^{3+} ions, respectively. The calculated value of J for $PrFeO_3$ (18.42 K) is greater than $PrCrO_3$ (9.43 K), which indicates the dilution of strength of superexchange interaction with the inclusions of Cr doping and results in the decrement of the values of T_{N1}. It can be mentioned here that the antiferromagnetic ordering temperature for $PrFeO_3$ is ~700 K [55], and with the incorporation of 50% Cr doping, T_{N1} reaches near RT. Hence, Cr^{3+} could be the best choice to replace Fe^{3+} to achieve superior magnetic properties. The advantage of Cr^{3+} substitution at the Fe^{3+} site is that T_{N1} can be achieved near RT, which scales the possibility of magneto-dielectric coupling and developing RT-based magnetodielectric devices [32,55].

Apart from T_{N1}, there is a peak in M-T data assigned as T_{N2}, which corresponds to the SR transition. Such transitions in the $RFe_{1-x}Cr_xO_3$ (R = rare earth atom) system arise due to complex exchange interactions between R^{3+} and Fe^{3+}/Cr^{3+} ions [55]. It is worth noting here that T_{N2} for the parent $RFeO_3$ is of the order of 50 K; however, with the inclusion of Cr doping [55], it systematically scales up to 150 K. The SR transition in $PrFeO_3$ takes place due to the domination of Pr^{3+}-Fe^{3+} interactions over the antiferromagnetic Fe^{3+}-Fe^{3+} interactions. The inclusion of Cr^{3+} ions at the Fe^{3+} site dilutes the Fe^{3+}-Fe^{3+} interactions, and Pr^{3+}-Fe^{3+}/Cr^{3+} interaction enhances, which may result in an increase in T_{N2} for Cr-substituted samples [22,32]. Walling *et al.* [59] explained the energy level diagram for a similar sample of $HoFeO_3$, and they reported that the ground-state pair (accidental doublet) of energy levels of Ho^{3+} is split by an energy difference of >80 cm^{-1} below the next higher level, and the anisotropic nature of the g factor pertinent to accidental doublet plays a crucial role in deciding the magnetism in these materials [19]. It also has been established that a low g factor would lead to an Ising axis for the rare earth moments in the *ab* plane at an angle of $\pm 63°$ with respect to the orthorhombic *a* axis [60]. Therefore, with the application of magnetic field Zeeman splitting takes place, which can split the accidental doublet and escalate the energy of the system parallel to the *ab* plane. Hence, the origin of T_{N2} can be explained in terms of the minimum energy configuration of spins which participate in the complex magnetic interactions. The SR transition observed in these samples is attributed to the transformation of
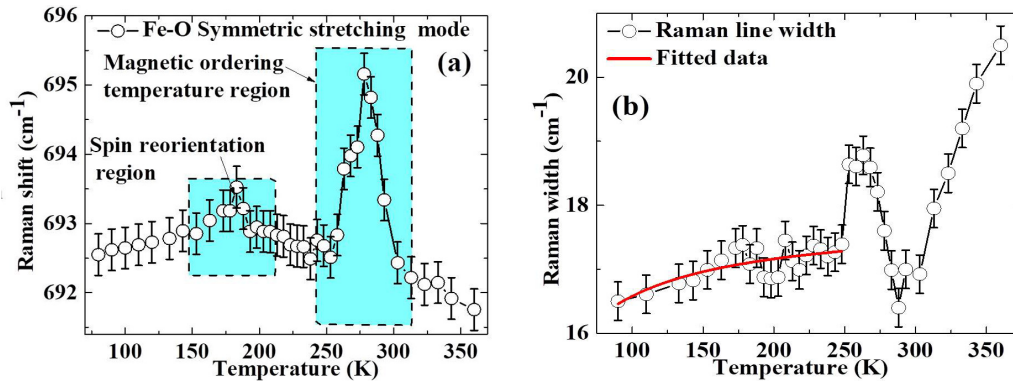
FIG. 2. (a) The Raman shift for the B_{2g} (7) mode and Fe-O symmetric stretching Raman mode as a function of temperature. (b) The variation of the Raman line width for B_{2g} (1) mode fitted by the Balkanski model. The deviation from normal anharmonic behavior suggests the presence of strong spin-phonon coupling/magneto-elastic coupling.

high-temperature T_4 ($G_x A_y F_z$) phase (high energy due to Zeeman splitting of accidental doublet) to T_2 ($F_x C_y G_z$) phase (low energy due to rotation of Fe^{3+} moments toward the c axis by $90°$) observed at low temperatures [22,59]. Apart from the T_{N1} and T_{N2}, the transition T_{N3} at low temperatures is clearly visible from Fig. 1. In the case of orthoferrites/orthochromites, this transition is basically attributed to the magnetic ordering of rare earth atoms and is reported in the literature with details [11–14]. It is well accepted that, around the magnetic transition region, the alignment of spins produces strain in the material due to magnetostriction, which causes a distortion in the lattice, and thus, magnetic ordering couples with phonon modes [32,55]. To confirm the same, TD Raman scattering experiments were carried out and will be elaborated in detail in the following sections.

C. TD Raman measurements

It is well established that RS can be employed as a microscopic tool to examine the variations in the structure, electron-phonon coupling, SPC, presence of defects, orbital mediated charge transfer, etc. [12,37,54,61]. The group theory analysis for the *Pnma* space group suggests the 24 Raman active modes with four formula unit per unit cell ascribed as [12]

$$7A_g + 5B_{1g} + 7B_{2g} + 5B_{3g}.$$

The Raman spectrum pertinent to $PrFe_{1/2}Cr_{1/2}O_3$ as a function of temperature is depicted in Fig. S07 (see Supplemental Material [40]). The detailed analysis of the Raman modes has been done in our recent publication [12] and is not discussed here. It is now well accepted that RS has the potential to investigate the structural changes and magnetic ordering with temperature [4,37]. The nonappearance/disappearance of any Raman mode in TD Raman spectra indicates the absence of any structural symmetry in the temperature range 90–350 K. Further, to get more insight into the effect of magnetic ordering temperature and spin-reorientation temperature on the phonon modes, Raman shift and full width at half maxima (FWHM) have been plotted and are depicted in Figs. 2(a) and 2(b). The anomalous behavior in Raman mode position and FWHM around T_{N1} and T_{N2} has been observed, which could be attributed to the presence of very high SPC across these

temperatures. Granado *et al.* [62] discussed the variation of Raman shift with temperature, and the shift is attributed to the factors ascribed below:

$$w(T) - w(0) = \Delta w_{lattice} + \Delta w_{sp-ph} + \Delta w_{anharmonic},$$

where $w(0)$ corresponds to the Raman shift at 0 K, $\Delta w_{lattice}$ gives the involvement of lattice volume contribution, Δw_{sp-ph} is the SPC contribution, and $\Delta w_{anharmonic}$ represents the anharmonic terms contribution. Since the $\Delta w_{lattice}$ denotes the contribution from the lattice volume due to thermal excitation of atoms and it deals with isotropic change in volume, it is not applicable here. This term represents the involvement of the change of the ionic binding energies due to the lattice expansion/contraction to the Raman shift and can be approximated by the Gruneisen law [62]: $(\frac{\Delta w_\alpha}{w_\alpha})lattice = \gamma_\alpha (\frac{\Delta V}{V})$. This equation is applicable for cubic crystals or for isotropically expanded lattices, and hence, it is not applicable here. Thus, the contribution due to $\Delta w_{lattice}$ is considered negligible.

Further, the anharmonic term contribution has been estimated by the Balkanski model expressed as [4,12]

$$T(T) = T(0) + A\left[1 + \Sigma \frac{1}{\exp\left(\frac{h\omega_i}{2\pi kT}\right) - 1}\right], \quad (2)$$

where $T(0)$ is the Raman FWHM at 0 K, and A (anharmonic coefficient) represents the contribution due to higher-order terms for three phonon processes. The dependency of Raman line width with temperature has been fitted by using the Balkanski model, and from the estimated values of A ($6\,cm^{-1}$) (for $T < 280\,K$), it can be concluded that the anharmonic term contribution is negligible, which is consistent with the earlier reported literature [4,12]. The deviation of Raman FWHM of B_{2g} (1) with temperature can be seen from Fig. 2(b), which suggests the presence of strong SPC around the magnetic transition temperature regions. Apart from this, the deviation of experimental data from the fitted Balkanski model [63] data $< T_{N1}$ indicates the presence of a dominating factor other than anharmonicity. Hence, it seems that the primary contributing factor for the anomalies observed in the TD Raman shift and FWHM is due to the presence of SPC, which may have a direct correlation with the observed magnetodielectric coupling. It is reported in the literature that the contribution of SPC in
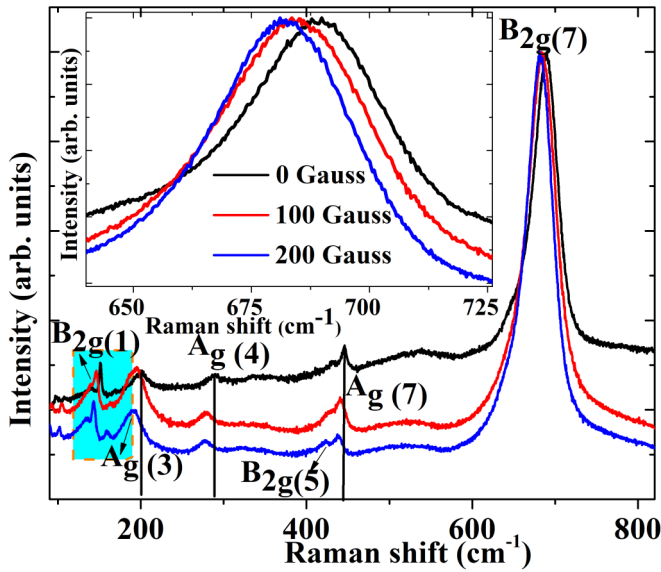
FIG. 3. The variation of Raman spectra as a function of the applied magnetic field. The inset of the figure represents the spin-phonon coupling induced magneto-expansion effect with the application of a magnetic field.

polarization (P) can be given as $P = \Delta Z M(T)/w(T)^2$, where w is the frequency of the phonon mode, M is the magnetization, and ΔZ is the effective charge [19]. This term arises due to the significant scattering experiments and could be very useful to understand the natural and magnetic field induced polar order, and this will be elaborated in detail in Sec. III D.

D. Effect of applied magnetic field on Raman line shapes at 290 K

To identify the intrinsic origin of magnetodielectric coupling, magnetic field-dependent Raman measurements have been carried out at 290 K. The detailed analysis of phonon modes assigned for the orthorhombic structure with space group *Pnma* was presented in our recent publications [37,64]. It is now well established that the samples which experience tensile strain undergo a redshift of Raman modes, which in the case of the system under investigation is further attributed to the increase in the Fe/Cr-O bond length. The Raman mode arising $\sim 690\,\mathrm{cm}^{-1}$ is related to symmetric stretching of the Fe/Cr-O bonds, whereas the soft A_g modes at lower wave number have a direct connection with the octahedral tilting. Figure 3 represents the magnetic field-dependent Raman spectra. It can be clearly seen that Raman spectra for $PrFe_{1/2}Cr_{1/2}O_3$ are highly affected by the applied small magnetic field. However, no significant changes have been observed for the parent $PrFeO_3$ sample (see Fig. S08 in Supplemental Material [40]), which reveals that SPC plays a crucial role in the observed magnetodielectric coupling. The Raman mode attributed to symmetric stretching vibrations of FeO_6 octahedra (690 cm^{-1} mode) shows the softening behavior or magneto-expansion with the field, which reveals that the Fe/Cr-O bond length is strongly affected by the magnetic field. In addition to this, the enhancement in the intensity of symmetric stretching vibrational mode (690 cm^{-1} mode) can

be seen from Fig. 3, which could be explained in terms of enhancement in the superexchange magnetic interactions by charge transfer from Cr^{3+} (d^3) to Fe^{3+} (d^5) ions [37]. Further, the soft A_g modes at lower wave number also show similar behavior, which could be attributed to the variation in the octahedral tilts with the magnetic field [34]. The variation of Raman shift as a function of applied magnetic field (H) for $PrFe_{1/2}Cr_{1/2}O_3$ at RT is tabulated in Table I. The systematic redshifting of the Raman modes with the application of magnetic field can be clearly seen from Table I, suggesting the magneto-expansion caused by the applied magnetic field.

Apart from this, the B_{2g} (1) Raman mode arising $\sim 160\,\mathrm{cm}^{-1}$ is related to the displacement of Pr^{3+} ions [32]. It is clear from the figure that a Raman spectrum for $PrFe_{1/2}Cr_{1/2}O_3$ is highly affected by the applied small magnetic field (100–200 Gauss), which is an indirect signature of magneto-dielectric coupling even at RT. It should be noted here that the signature of magneto-dielectric coupling is completely missed in $PrFeO_3$, as depicted in Fig. S08 (see Supplemental Material [40]). Hence, it can be concluded that Pr^{3+} ions in $PrFeO_3$ are highly localized, whereas with the inclusion of Cr substitution, Pr^{3+} ions get delocalized and would contribute significantly to magneto-dielectric coupling. The distortion of the Pr^{3+} ion due to the Pr-Fe/Cr exchange field seems to be responsible for the displacement of the Pr^{3+} ion, i.e., the polyhedral formed around the Pr^{3+} ion is no longer centrosymmetric and results in producing a local dipole. Hence, it seems that the anomalies in the low-frequency modes related to the Pr ion motion and the presence of SPC supports the claim that the coupling between $4f$-$3d$ moments plays a vital role in inducing switchable electric polarization. Many mechanisms for overcoming the contraindication between the d^0-ness that favors ferroelectricity and the d^n occupation required for magnetism have been identified over the last decades [8,65]. In the case of ferroelectric materials such as $BaTiO_3$ or $SrTiO_3$, the ferroelectricity can be understood in terms of centered distortion of TiO_6 octahedra around Ti^{4+} ions. The Ti^{4+} ions play an important role in deciding the ferroelectric behavior, whereas the importance of the present investigations lies in the fact that R site ions (Pr^{3+} ions) play an important role in deciding the ferroelectric behavior in orthoferrites/orthochromates.

On the other hand, the origin of SPC induced magnetodielectric coupling has been explained in terms of rotation of spin-coupled Fe orbitals under the influence of the magnetic field. The application of magnetic field aligns or rotates magnetic moments associated with sublattices; hence, readjustment/rerotation of already rotated/adjusted orbitals can take place (as strong spin-orbital coupling in such correlated systems is quite known), which may result in a change in orthorhombic strain or in cell volume (i.e., expansion or contraction of material), and hence in capacitance (or ε') according to the relation $C = \varepsilon_0 \varepsilon' \frac{A}{d}$ [3], where ε_0 is the dielectric permittivity of free space, ε' is the dielectric permittivity or dielectric constant of the material filled between the electrodes, d is the thickness of material, and A is the area of the contact plates. Hence, as a final remark, this paper reveals that the intrinsic magnetodielectric effect can be realized in strongly correlated compounds that contract/expand in response to an externally applied magnetic field. These results are in

TABLE I. The variation of Raman mode as a function of applied magnetic field (H) for $PrFe_{1/2}Cr_{1/2}O_3$ at RT.

Raman mode	Raman shift with $H = 0$ Gauss	Raman shift with $H = 100$ Gauss	Raman shift with $H = 200$ Gauss
B_{2g} (7)	690.62 ± 0.35	685.49 ± 0.35	681.43 ± 0.35
A_g (7)	446.45 ± 0.35	442.69 ± 0.35	435.55 ± 0.35
B_{2g} (5)	432.52 ± 0.35	429.55 ± 0.35	426.62 ± 0.35
A_g (3)	200.47 ± 0.35	194.26 ± 0.35	191.45 ± 0.35
B_{2g} (1)	151.72 ± 0.35	146.52 ± 0.35	143.39 ± 0.35

excellent agreement with the results published by Rajeswaran *et al.* [13,22], where polarization is changing systematically with the strength of the applied magnetic field. Therefore, it can be concluded that, at low temperatures, the Pr atomic displacement has a significant contribution to the observed polar order. These results have been predicted theoretically by various research groups that the delocalizing nature of the A site ions in ABO_3 perovskites could be responsible for the origin of natural polar order, and these results can be an indirect experimental proof of earlier predicated theoretical results [66,67].

E. Possible origin of Pr atoms delocalization as a function of temperature and its role in natural and field induced polar order

To understand the possible origin of delocalization of Pr atoms and its role in the natural and magnetic field induced polar order, the magnetic field-dependent Raman scattering experiments as a function of temperature were performed by applying a very small magnetic field (30 Gauss) [68]. It is worth mentioning here that the applied magnetic field was so small that it does not lead to any change in the Raman spectra at RT. The corresponding Raman spectrum at 90 K with the application of the magnetic field is depicted in Figs. 4(a) and 4(b). It is evident from the figure that the visible Raman shift of the order of $2 cm^{-1}$ in the low wave number Raman mode ($160 cm^{-1}$) has been observed at 90 K, whereas no significant changes in all other Raman modes corresponding to Fe ($>440 cm^{-1}$) vibrations have been observed, as is clear from the Fig. 4(b). It is important to note here that the Raman modes $<440 cm^{-1}$ are attributed to the heavier Pr atom vibrations [12], and the deviation of only these modes with applied magnetic field reveals that the large values of $\Delta\varepsilon$ (a detailed discussion is given in Sec. III.9) at low temperatures have a direct relationship with the displacement of Pr atoms. Importantly, in this context, the polarization (P) is proportional to the displacement of the soft B_{2g} (1) mode [69] (i.e., $P = T w_{160}$, where T is a constant of proportionality, and w_160 is the Raman shift of the particular mode). This qualitative relation would lead to the following simplified expression for the magnetic field induced polarization relation [58,69]:

$$\frac{P(H) - P(0)}{P(0)} \propto \frac{W(H) - W(0)}{W(0)}. \quad (3)$$

To get further insight, the TD Raman shift for B_{2g} (1) mode attributed to the displacements of Pr sublattices and the A_g (7) mode was plotted without and with a small magnetic field. Both spectra are plotted in Figs. 4(c) and 4(d), respectively. It is clear from Fig. 4(c) that Δw (the difference between Raman shifts with and without magnetic field) decreases

systematically with increase in temperature, and at RT, it almost vanishes, suggesting a strong magnetodielectric coupling at low temperatures [59]. Also, no significant changes have been observed in the Raman shift corresponding to Fe vibrations [A_g (7)] with the application of magnetic field, which suggests that the Fe atoms do not contribute significantly to the field induced polar order even at low temperatures. Thus, the softening of the low wave number Raman modes with magnetic field in $PrFe_{1/2}Cr_{1/2}O_3$ demonstrates the magnetic field induced electric polarization by stress-mediated magnetodielectric coupling [68], which is consistent with the variation of Δw and $\Delta\varepsilon$ (estimated from TD dielectric measurements), as shown in Fig. 4(e).

Further, the contribution due to Pr atom displacement in the natural polar order can be explained as follows: The actual lattice symmetry of the sample is lower than the usually assumed *Pnma* due to presence of undetected distortion. The Pr ions in the *Pbnm* structure are not lying at the center of symmetry; their point group is C_s not D_{2h}. These Pr ions lie in the mirror plane perpendicular to the c axis, and the coordinates of Pr ions in the ab plane are not fixed. Thus, Pr atoms might be displaced to produce a local dipole [23]. However, Pr ions could be opposite and cancel the dipoles in the *Pbnm* symmetry. If the real symmetry of the lattice (and consequently the point symmetry of the Pr ion) would be lower, these contributions would not cancel and could give ferroelectric polarization below magnetic transition temperature. Such a small noncentrosymmetry cannot be probed using XRD experiments due to their limitation of probing the global structure [54].

Therefore, the importance of these results are (i) contribution of Pr^{3+} ions in the natural and magnetic field induced polar order; (ii) to use Raman scattering as an alternative tool to probe these polar orders; and (iii) the changes in the Fe-O bond length (>30 Gauss) signify that Fe atoms are also playing a role in the magnetic field induced polar order, and for $H < 30$ Gauss, the role of Pr^{3+} ion displacement becomes more important. These results show excellent conformance with the NCS and NRTA, as discussed in detail in the following sections.

F. INS, NCS, and NRTA analysis

To shed more light on the delocalization of the Pr^{3+} ions, isotopic mass-resolved NCS, augmented with NRTA, as well as INS experiments were performed on $PrFe_{1/2}Cr_{1/2}O_3$ and $PrFeO_3$. An example of a mass-resolved NCS spectrum recorded in the TOF domain for $PrFe_{1/2}Cr_{1/2}O_3$ and $PrFeO_3$ at $T = 10$ K is shown in Figs. 5(a) and 5(b), respectively. As routinely applied for the analysis of the NCS spectra of
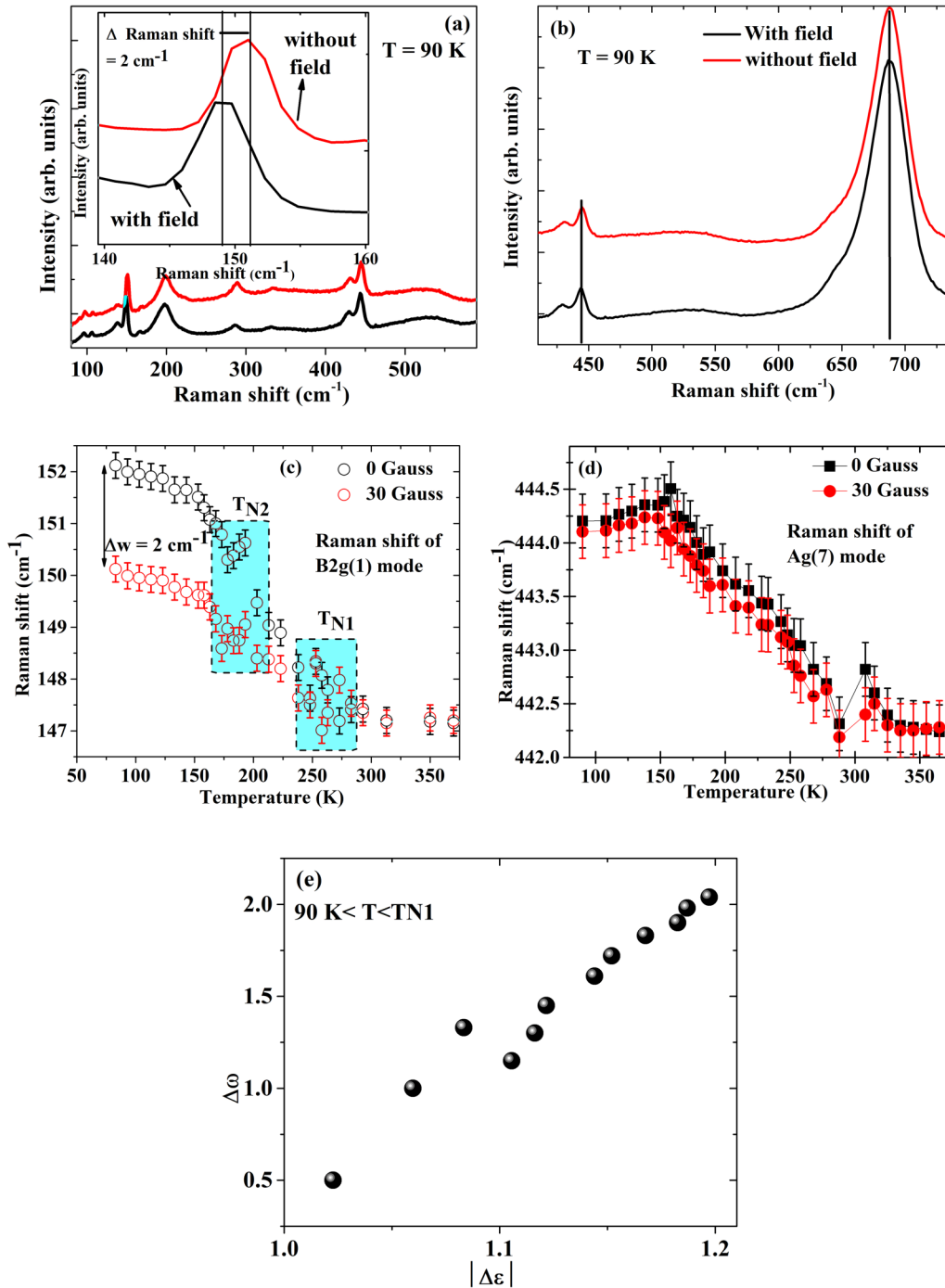
FIG. 4. The low-temperature Raman spectra (90 K) related to (a) Pr atomic vibrations and (b) Fe atomic vibrations recorded with and without the application of a very small magnetic field (30 Gauss). The Raman shift at 90 K with the magnetic field applied is maximized for heavier Pr atomic vibrations, suggesting the involvement of Pr atomic displacements in observed polar order. (c) and (d) The variation of Raman shift as a function of temperature for B_{2g} (1) and A_g (7) modes with the application of the magnetic field. The changes of the Raman shift of B_{2g} Raman mode with the application of magnetic field reveal that the field induced polar order at low temperatures has a direct relationship with the displacement of Pr atoms. (e) The variation of Δw (variation in Raman shift with the application of magnetic field) vs $\Delta \varepsilon$ (variation in dielectric constant due to the presence of hyperfine interactions).

samples composed of heavyweight nuclei [44], the total neutronic responses of both samples were fitted with underlying Gaussian nuclear momentum distributions convolved with the isotopic mass-dependent resolution functions. As mentioned in Sec. II B 4, the technique of stoichiometric fixing [40] was applied in fitting NCS spectra, which allowed for reliable

fitting of the widths of the recoil peaks despite their partial overlapping in the signals recorded in the TOF domain [see Figs. 5(a) and 5(b)]. Following the rule of thumb on the inverted-geometry NCS spectrometers, the recoil peaks appear centered at increasing values of the TOF for the increasing masses of individual nuclear species.
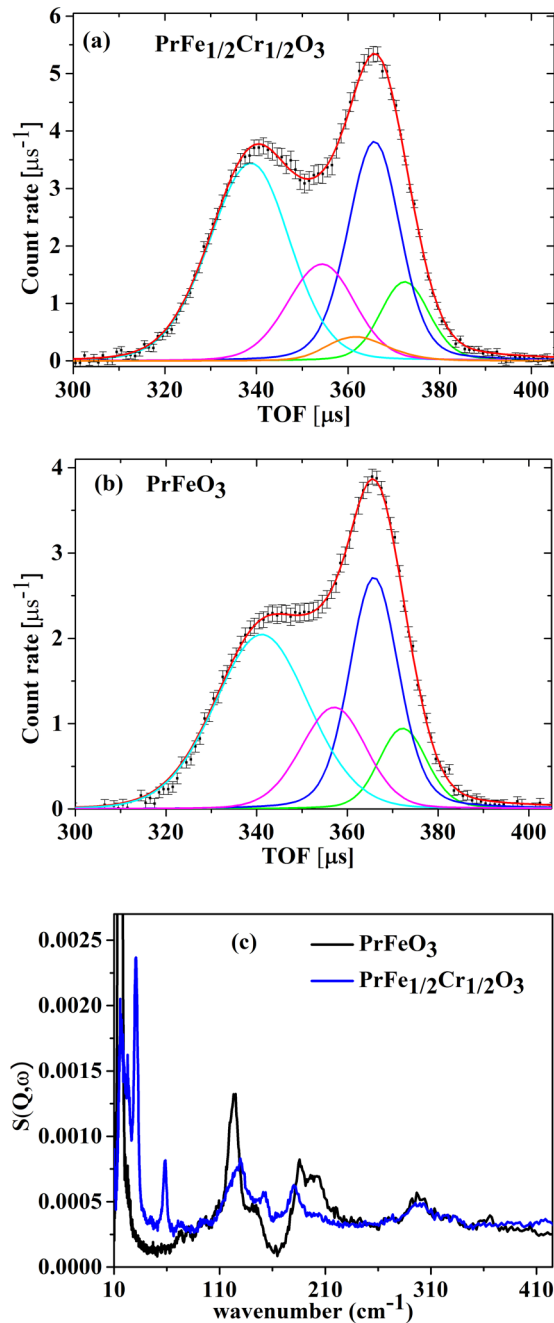
FIG. 5. Neutron Compton scattering (NCS) spectrum for (a) Cr-substituted $PrFeO_3$ and (b) $PrFeO_3$, both recorded at 10 K. Black points show the sum (over all backward scattering detectors) of the recorded data. A solid red curve indicates the sum (over all backward scattering detectors) of the fits of the recorded data. The sum of the fits is dissected into sums (over all backward detectors) of fits to individual recoil lines of Pr (solid green line), Fe (solid navy blue line), Cr (solid orange line), aluminum sample container (magenta), and O (solid blue line). (c) Inelastic neutron scattering (INS) spectra of Cr-substituted $PrFeO_3$ (solid blue line) and $PrFeO_3$ (solid black line). The contribution from the sample aluminum container has been subtracted, and the resultant spectra were normalized/scaled in such a way that the integrated area between 10 and 4000 cm^{-1} is equal to 1.

In Fig. 5(a), these are the recoil peak of the oxygen, aluminum sample container, chromium [absent for $PrFeO_3$—see Fig. 5(b)], iron, and praseodymium, all Doppler broadened by their respective nuclear momentum distributions. The widths (standard deviations), denoted as σ, of the Gaussian nuclear momentum distributions underlying the Doppler-broadened recoil peaks of individual nuclear species present in $PrFe_{1/2}Cr_{1/2}O_3$ and $PrFeO_3$ are listed in Table II.

As can be clearly seen in Table II, the values of the widths of momentum distributions of Pr in $PrFe_{1/2}Cr_{1/2}O_3$ are smaller than $PrFeO_3$, both at $T = 10$ and 300 K. By virtue of the uncertainty principle, the narrower the momentum distribution, the more a given species is delocalized in space [42–44]. Thus, the Pr^{3+} ions seem to be more delocalized in space in $PrFe_{1/2}Cr_{1/2}O_3$ than their counterparts in $PrFeO_3$, and this delocalization seems to be more markedly manifested at $T = 10$ K than RT. Interestingly, an inverse trend is visible in the case of the Fe^{3+} ions, also more manifested at $T = 10$ K than RT. For oxygen, no marked differences are observed between both compounds at both temperatures.

Moreover, a more careful inspection reveals quite marked and important differences between the two compounds. Firstly, as a rule of thumb according to the classical limit of quantum mechanics, the heavier the nuclear species under consideration, the more "classical or localized in space" it should be. Thus, an expected natural progression of the widths of nuclear momentum distributions at any given constant temperature should be such that the heavier the species, the wider its momentum distribution gets. Conversely, the widths of nuclear momentum distributions should be approximately equal for two nuclear species of equal masses at the same temperature in the classical limit. As can be seen by inspection of the results listed for $T = 300$ K for both compounds, this trend is approximately fulfilled at 300 K, where, as expected, the nuclear quantum effects for heavyweight nuclei start to cease, and the momentum distributions become more and more similar to Maxwell-Boltzmann distributions of classical noninteracting particles subject to no confinement [41–44]. However, at $T = 10$ K, a completely different picture emerges. The Pr nuclei, whose mass is approximately three times higher than the mass of the Fe nuclei, have the momentum distribution width that is $\sim 50\%$ narrower than that of iron and even lower than the width of the momentum distribution of the approximately ten times lighter oxygen nucleus. Interestingly, the same trend is visible in the case of chromium nuclei, for which the mass difference with respect to oxygen and iron is not so dramatic as in the case of praseodymium, however. To provide a degree of quantitation to these trends, an observable referred to as the quantum excess (QE) of the nuclear kinetic energy [41–44] has been introduced. The QE $= E_{quant}/E_{cl}$ measures the "quantumness" of a given nuclear species of mass M. QE is defined as the ratio of the nuclear kinetic energy $E_{quant} = 3\hbar^2\sigma^2/2M$ measured in an NCS experiment to E_{cl}, which is the nuclear kinetic energy of a classical nucleus subject to no confining potential (and thus given by the Maxwell-Boltzmann distribution) $E_{cl} = \frac{3}{2}kT$. The values of the QE calculated for all nuclear species present in $PrFe_{1/2}Cr_{1/2}O_3$ and $PrFeO_3$ are listed in Table III.

TABLE II. The widths (standard deviations), denoted as σ, of the Gaussian nuclear momentum distributions underlying the Doppler-broadened recoil peaks of individual nuclear species present in PrFe$_{1/2}$Cr$_{1/2}$O$_3$ and PrFeO$_3$ (see text for details).

Sample	σ(Pr)(Å^{-1})	σ(Fe)(Å^{-1})	σ(Cr)(Å^{-1})	σ(O)(Å^{-1})
PrFe$_{1/2}$Cr$_{1/2}$O$_3$ $T = 10$ K	5.9 ± 0.1	10.3 ± 0.5	4.1 ± 0.3	8.9 ± 0.5
PrFe$_{1/2}$Cr$_{1/2}$O$_3$ $T = 300$ K	30 ± 2	21 ± 2	18 ± 2	11 ± 1
PrFeO$_3$ $T = 10$ K	6.2 ± 0.1	7.9 ± 0.5		9.0 ± 0.5
PrFeO$_3$ $T = 300$ K	34 ± 2	19 ± 2		11 ± 1

As can be clearly seen from the inspection of Table III, the value of the QE of praseodymium in PrFe$_{1/2}$Cr$_{1/2}$O$_3$ is closer to unity than the QE value for Pr in PrFeO$_3$, both at $T = 10$ and 300 K. A value of QE closer to unity signifies a more classical character of an atomic species, whereby it resembles more a nucleus that is unconfined or not subject to any local binding potential and thus delocalized [42]. Moreover, the praseodymium seems to be much more classical (unconfined) in PrFe$_{1/2}$Cr$_{1/2}$O$_3$ at $T = 10$ K than the three times lighter iron nucleus and ∼10 times lighter oxygen nucleus.

The picture of the increased degree of delocalization of the Pr^{3+} ion in PrFe$_{1/2}$Cr$_{1/2}$O$_3$ compared with its counterpart in PrFeO$_3$ emerging from the analysis of the NCS data is further corroborated by the INS results on PrFe$_{1/2}$Cr$_{1/2}$O$_3$ and PrFeO$_3$ obtained at $T = 10$ K [see Fig. 5(c)]. To understand this result, it is worth noting that the nuclear kinetic energy can be interpreted as the first moment of the Boltzmann population factor-weighted partial (atom projected) vibrational density of states (apVDOS) [41–44]. For a constant temperature experiment, this interpretation means that the nuclear kinetic energy of a nucleus is roughly given by the value of the center of the gravity of a region of a vibrational spectrum that is dominated by the partial apVDOS of this nucleus. The detailed analysis of phonon modes for an orthorhombic structure with space group *Pnma* [37,64] reveals two main modes related to the apVDOS of the A^{3+} ions, the A$_g$ (2) and B$_{2g}$ (1) modes. The main atomic motion is of the type of A(z) out of plane and A(x) motion, for the first and second modes, respectively [32]. In the case of HoCrO$_3$ and HoCr$_{0.5}$Fe$_{0.5}$O^3 [32], the first mode is in the region of 140 cm^{-1} and the second one in the region of 160 cm^{-1}. The closest vibrational peaks present in the INS spectrum of PrFe$_{1/2}$Cr$_{1/2}$O$_3$ and PrFeO$_3$ obtained at $T = 10$ K are visible at ∼ 135 and ∼185 cm^{-1}, respectively [see Fig. 5(c)]. Thus, for the assessment of the center of gravity (CoG) of the apVDOS of praseodymium in PrFe$_{1/2}$Cr$_{1/2}$O$_3$ and PrFeO$_3$, a spectral region between 120 and 240 cm^{-1} was chosen. The apVDOS of praseodymium was obtained from the total inelastic structure factor $S(Q,\omega)$, recorded at TOSCA, applying the procedure by Colognesi

et al. [70]. In this procedure, an approximation is made that $S(Q,\omega)$ in a chosen frequency range can approximate the self-structure factor $S_S^{(A)}(Q,\omega)$ pertaining to nucleus A. This assumption rests on several approximations. Firstly, the harmonic lattice approximation is assumed. Secondly, it is assumed that the contributions from multiple scattering to $S(Q,\omega)$ are negligible. Finally, the inelastic structure factor, measured in an experiment, is assumed to have negligible multiphonon contributions, and thus, $S_S^{(A)}(Q,\omega)$ is effectively related only to the single-phonon transitions, from which an apVDOS can be extracted in a straightforward manner. In the zeroth iteration of this procedure, an apVDOS of a nucleus A, $Z_A^{(1)}(\omega)$, can be related to $S_S^{(A)}(Q,\omega)$ using the following formula:

$$CZ_A^{(1)}(w) = \frac{4M}{h} \frac{\omega}{Q_{TSC}^2(\omega)} \left[\coth\left(\frac{\hbar\omega}{2kT}\right) + 1 \right]^{-1}$$
$$\times \exp\left[\frac{\langle u^2 \rangle_A^{(0)} Q_{TSC}^2(\omega)}{3} \right] C S_S^{(A)}[Q_{TSC}(\omega), \omega]. \tag{4}$$

Based on this formula, the following procedure was applied. First, the magnitude of the neutron momentum transfer along the instrument trajectory $Q_{TSC}(\omega)$ was approximated by the recoil equation of hydrogen $Q_{TSC}(\omega) \simeq \sqrt{2M_H \omega/\hbar^2}$, a well-known approximation for an inverse-geometry spectrometer with a final neutron energy value negligible compared to the measured neutron energy transfer [47]. Then the Debye-Waller factor $\exp[\langle u^2 \rangle_A^{(0)} Q_{TSC}^2(\omega)/3]$ was computed for a chosen spectral region using as $\langle \mathbf{u}^2 \rangle_A^{(0)}$ the values of isotropic displacement parameters U_{iso} obtained from our XRD study of PrFe$_{1/2}$Cr$_{1/2}$O$_3$ and PrFeO$_3$. The values of U_{iso} were 0.0154(3) and 0.0146(3) Å^2, respectively. It is worth mentioning here that the values of U_{iso} obtained in our XRD analysis have a direct connection to the amount of delocalization of the Pr^{3+} ion, and their direct inspection leads to the conclusion about a greater degree of spatial delocalization of the Pr^{3+} ion in PrFe$_{1/2}$Cr$_{1/2}$O$_3$ than PrFeO$_3$, independent

TABLE III. The values of the QE variable measuring the "quantumness" of individual nuclear species present in PrFe$_{1/2}$Cr$_{1/2}$O$_3$ and PrFeO$_3$ (see text for details).

Sample	QE (Pr)	QE (Fe)	QE (Cr)	QE (O)
PrFe$_{1/2}$Cr$_{1/2}$O$_3$ $T = 10$ K	1.2 ± 0.1	9.2 ± 0.6	1.6 ± 0.4	24 ± 3
PrFe$_{1/2}$Cr$_{1/2}$O$_3$ $T = 300$ K	1.0 ± 0.1	1.5 ± 0.2	1.3 ± 0.2	1.5 ± 0.2
PrFeO$_3$ $T = 10$ K	1.3 ± 0.1	5.4 ± 0.6		25 ± 3
PrFeO$_3$ $T = 300$ K	1.3 ± 0.2	1.0 ± 0.2		1.2 ± 0.2

of the conclusions from the NCS and INS data analysis. Following the evaluation of the Debye-Waller factor, the factor $\frac{\omega}{Q_{TSC}^2(\omega)}[\coth(\frac{\hbar\omega}{2kT})+1]^{-1}$ was computed in the entire chosen spectral region. Finally, the CoG of $Z_A^{(1)}(\omega)$ was computed according to the formula $\int \omega Z_A^{(1)}(\omega)d\omega / \int Z_A^{(1)}(\omega)d\omega$. It is worth mentioning here that, by virtue of the calculation of the CoG, the factor $\frac{4M}{\hbar}$, containing the mass of the praseodymium M and the normalization constant C, becomes redundant as they cancel out. The values of the nuclear kinetic energy of praseodymium obtained from the procedure described above are 4.00 ± 0.05 meV and 3.90 ± 0.05 meV for $PrFeO_3$ and $PrFe_{1/2}Cr_{1/2}O_3$, respectively. From these values, the values of the widths of momentum distributions of praseodymium yield 9.48 ± 0.04 and 9.36 ± 0.04 for Pr in $PrFeO_3$ and $PrFe_{1/2}Cr_{1/2}O_3$, respectively.

To further corroborate the finding from the analysis of the XRD, INS, and NCS data, the NRTA was performed on both systems at $T = 10$ and 300 K. Before we proceed to the discussion of the results, it is worth mentioning that the VESUVIO spectrometer, in its present configuration, is equipped with the possibility of recording both NRTA (in the transmission mode) and neutron resonant capture analysis (in the scattering mode). After a careful analysis of the spectra of $PrFe_{1/2}Cr_{1/2}O_3$ and $PrFeO_3$ recorded at VESUVIO, a choice was made to employ the NRTA technique. The reason behind such a choice was that, in the case of spectra recorded in transmission mode, the Doppler-broadened neutron resonances are present in NRTA spectra as dips because neutrons have traversed the samples with no interaction with it. In consequence, unlike in the case of the neutron resonant capture analysis, the NRTA data are free from the effects of multiple scattering and scattering followed by resonant absorption, which greatly simplifies the data analysis and increases the precision and resolution with which the values of nuclear kinetic energy are extracted from the Doppler broadening of the absorption resonances. Figure 6 shows the NRTA spectra of Pr141 resonances of $PrFe_{1/2}Cr_{1/2}O_3$ and $PrFeO_3$ recorded at (a) $T = 10$ K and (b) $T = 300$ K. Bearing in mind that the energy resolution in NRTA decreases with increasing neutron energy, three resonant peaks were selected in the low-energy region of the resonant neutron absorption spectra. The resonance energies of these peaks were identified as 218.7, 235,2 and 359.5 eV, according to the tabulated data deposited in the ENDF/BVII.0 database [71]. Already at first glance, all three peaks present in the NRTA spectra of $PrFe_{1/2}Cr_{1/2}O_3$ are markedly narrower (show less Doppler broadening) than the peaks in $PrFeO_3$. Thus, from the inspection of the raw NRTA data, it is apparent that the Pr^{3+} ions in $PrFe_{1/2}Cr_{1/2}O_3$ are less Doppler broadened (more delocalized in space) than their counterparts in $PrFeO_3$.

The peaks present in the NRTA spectra of Cr-substituted $PrFeO_3$ and $PrFeO_3$ were fitted globally with the profile being a convolution of the resolution function and Doppler-broadened Breit-Wigner resonance curves with the amount of Doppler broadening (nuclear kinetic energy) as a shared global parameter. The results of the fits are shown in Fig. 7 and Table IV. In Table IV, according to the procedure already established in the NRCA work on gold resonances [37], the values of the nuclear kinetic energy of praseodymium are
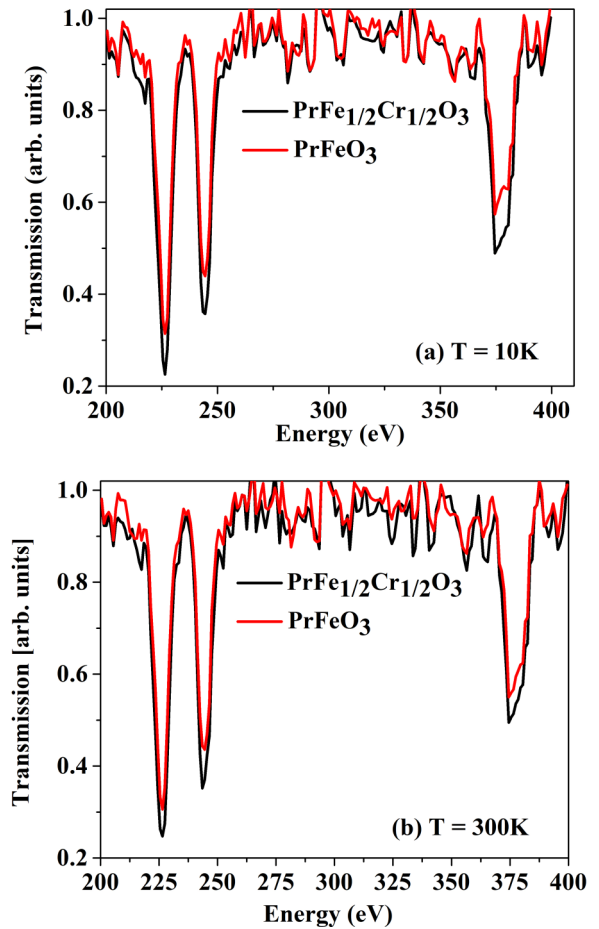

FIG. 6. (a) Neutron resonance transmission analysis (NRTA) spectra of Pr141 resonances of $PrFe_{1/2}Cr_{1/2}O_3$ and $PrFeO_3$ recorded at $T = 10$ K. (b) NRTA spectra of Pr141 resonances of $PrFe_{1/2}Cr_{1/2}O_3$ and $PrFeO_3$ recorded at $T = 300$ K. See text for details.

expressed in terms of effective temperatures T^* a representation of data that suits very well the calculation of the QE variable, which can also be defined as $QE = T^*/T$, where T is the thermodynamic temperature. Inspections of Tables III and IV show that results of the analysis of the NCS data of the praseodymium are corroborated, both qualitatively and quantitatively, by the results of the NRTA data. This is an important result, considering that the NRTA technique resolves the praseodymium nuclear species in an isotope-selective manner and is free of any systematic errors due to peak overlap that is characteristic of the NCS method.

Overall, the main result of the analysis of $PrFe_{1/2}Cr_{1/2}O_3$ and $PrFeO_3$, the chromium induced increased spatial delocalization of the Pr^{3+} ions, is jointly corroborated by XRD, INS, NCS, and NRTA methods. Despite the same trend present in data obtained from the four methods, there are some quantitative differences. First, assuming Gaussian momentum and position distributions and using the uncertainty principle between the momentum and position, expressed in our system of units as [70] $\langle u^2 \rangle \langle p^2 \rangle = \frac{3}{4}$, one obtains from the values of U_{iso} obtained in our XRD analysis the values of the widths (standard deviations) of momentum distributions $\sqrt{\langle p^2 \rangle}$ equal to 7.16 and 6.98 Å^{-1} for $PrFeO_3$ and $PrFe_{1/2}Cr_{1/2}O_3$,
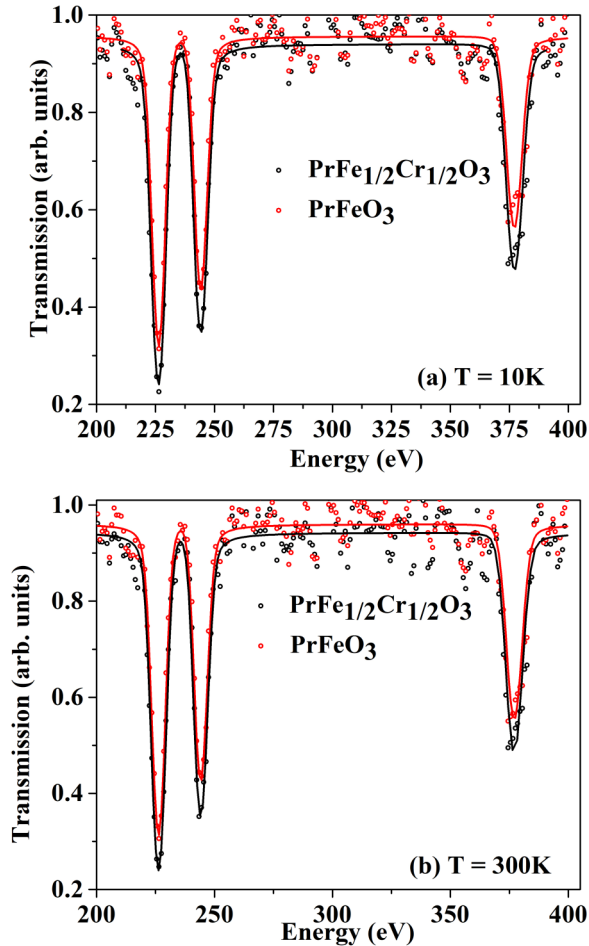
FIG. 7. Neutron resonance transmission analysis (NRTA) spectra of Pr141 resonances of $PrFe_{1/2}Cr_{1/2}O_3$ and $PrFeO_3$ recorded at (a) $T = 10$ K and (b) $T = 300$ K together with fits. See text for details.

TABLE IV. The values of the effective temperatures $T*$ and QE variable of the praseodymium in $PrFe_{1/2}Cr_{1/2}O_3$ and $PrFeO_3$ obtained from the NRTA fits (see text for details).

Sample	$T*$(Pr) (K)	QE (Pr)
$PrFe_{1/2}Cr_{1/2}O_3$ $T = 10$ K	12 ± 1	1.2 ± 0.1
$PrFe_{1/2}Cr_{1/2}O_3$ $T = 300$ K	300 ± 30	1.0 ± 0.1
$PrFeO_3$ $T = 10$ K	13 ± 1	1.3 ± 0.1
$PrFeO_3$ $T = 300$ K	390 ± 60	1.3 ± 0.2

does not decrease with increasing energy transfer of neutrons but rather with the increasing mass of the recoiling nuclear species. Thus, if it were not for the fact that the protocol applied to extract the values of nuclear kinetic energies from the INS data relies on several approximations that are absent in the data analysis from NCS experiments, it would have been the INS data that would have given the most precise estimate of the delocalization of the Pr^{3+} ion. However, the fact that the results of the NRTA and NCS data analysis are identical lets us believe that the quantitative results obtained by them are the most reliable. Taken together, despite some numerical inaccuracies and discrepancies between the values of observables pertaining to the nuclear delocalization of praseodymium obtained through different techniques, the qualitative result of the global analysis is significant, as the same trend is present in all types of data.

G. TD dielectric measurements

The TD dielectric measurements were performed to understand the presence of magnetodielectric coupling, and the corresponding results are depicted in Fig. 8(a) at the frequency of 1 MHz. It can be seen from the figure that, around the magnetic ordering temperature, a clear anomaly was observed in the permittivity data. Moreover, the first derivative of the ε vs T curve [as depicted in the inset of Fig. 8(a)] confirms that the anomaly takes place at ~ 280 K. The dielectric anomaly in the form of a cusp around the magnetic transition temperature reveals the possibility of observing the magnetodielectric effect very close to RT. The said cusp-type characteristics were also observed in $GaFeO_3$ [72] and $YMnO_3$ [21], which have been explained in terms of the presence of the magnetodielectric effect. Hence, the observed behavior is attributed to the antiferromagnetic ordering from the superexchange interactions between the Fe^{3+}/Cr^{3+} ions. It is worth noting here that, in the absence of magnetic ordering, the dielectric constant varies similarly as in the high-temperature region (>280 K). However, because of the presence of internal hyperfine magnetic field interactions <280 K, the dielectric permittivity below this temperature cannot follow the same trend. Therefore, the variation of low-temperature dielectric constant in the absence of zero hyperfine magnetic fields can be obtained by extrapolating the high-temperature window region.

The difference $\Delta \varepsilon$ between the ε_0 (zero field ε in the low-temperature region) and ε (the experimental value of field ε in the low-temperature region) would only be the result of magnetic hyperfine interactions and could be proportional to the square of magnetization [2], i.e., $\Delta \varepsilon \approx M^2(T)$. The variation of $\Delta \varepsilon$ as a function of M^2 is depicted in Fig. 8(b). The

respectively. These values are larger than the values obtained from the analysis of the NCS data by ~ 1 Å^{-1} and ~ 2.3 Å^{-1} lower than the values obtained from the analysis of the INS data. The discrepancy between the values obtained from the NCS and XRD data analysis is related to the fact that both methods are sensitive to a completely different type of atomic motions. Whereas, as discussed above, the NCS is mostly sensitive to high-frequency atomic vibrations as it measures the widths of momentum distributions related to the first moments of apVDOS, the U_{iso} values obtained from diffraction data analysis are sensitive to low-frequency atomic motions, as they are determined by the minus-first moments of apVDOS [70]. Moreover, the INS method, as implemented at an inverse-geometry spectrometer like TOSCA, is most sensitive and precise in the case of measuring low- to medium-frequency atomic motions due to the fact that both the instrument resolution and the Debye-Waller factor [see Eq. (4)] deteriorate the quality of an INS spectrum more the higher the frequency is measured. Thus, the spectral range between 120 and 240 cm^{-1}, selected for the extraction of the values of the nuclear kinetic energy of praseodymium, is the one in which TOSCA spectra are recorded most precisely. Unlike INS, in the case of NCS, the resolution of the technique
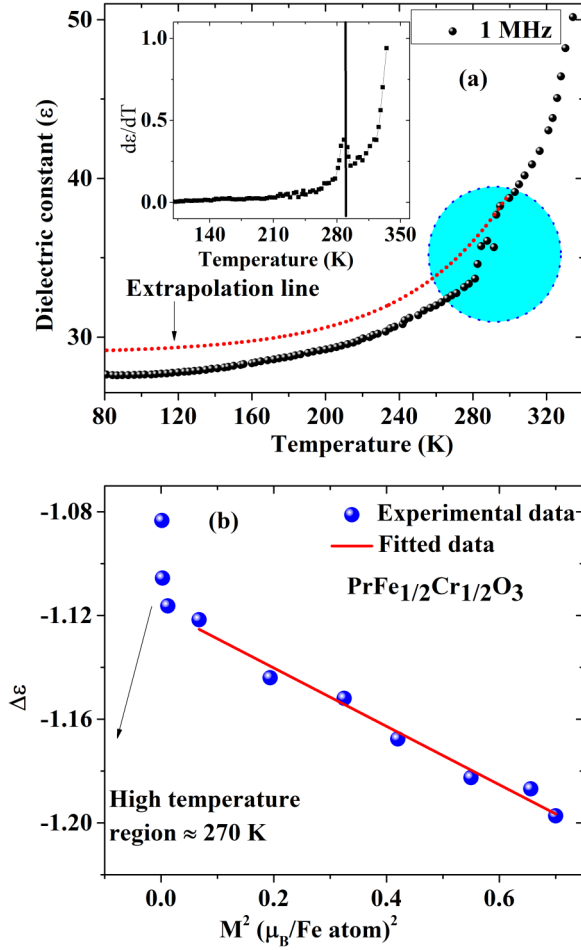
FIG. 8. (a) The temperature dependence of dielectric constant variation at 1 MHz. The inset of the figure represents the first derivative of dielectric constant with temperature. The anomaly near 280 K is attributed to the presence of magnetodielectric coupling. (b) The linear variation between the $\Delta\varepsilon$ and $M^2(T)$. The deviation of normal linear behavior could be attributed to internal magnetic hyperfine interactions.

linear variation of M^2 in the temperature window 150–280 K can be seen from Fig. 8(b); however, this linear dependence deviates ∼280 K because of magnetodielectric coupling. These results show excellent consistency with the magnetic field-dependent Raman scattering experiments. Hence, it seems that the present results show a significant contribution in searching for RT-based magnetodielectric materials.

As far as intrinsic magnetodielectric (MD) coupling is concerned, ideally, it can be realized in a material with magnetically switchable net electric dipole moment, and such systems are barely formed. Nonetheless, it can be achieved by making a compound that expands/shrinks in response to an externally applied magnetic field as the capacitance C is related to the dimensions of the sample by the following relation [3]:

$$C \propto A/d,$$

where C is the capacitance of a dielectric material, A the area, and d is the thickness of the dielectric. The detailed analysis of
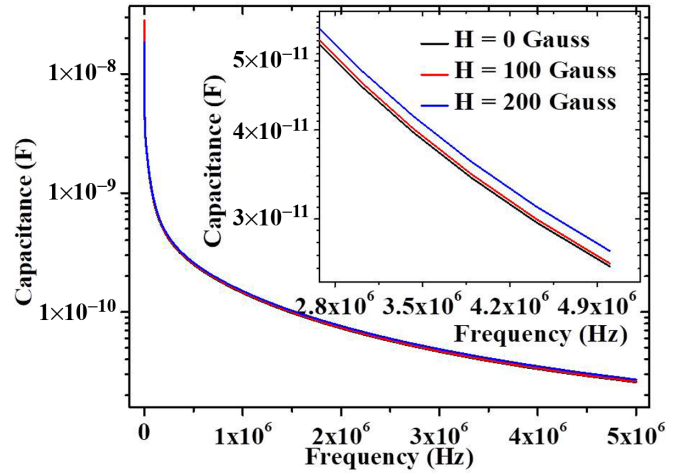

FIG. 9. The variation of capacitance as a function of the magnetic field.

the expansion of the material with the applied magnetic field is already discussed in the earlier sections; however, its impact on the ε' as a function of the applied magnetic field is depicted in Fig. 9. It can be seen from the figure that ε' can be tuned with the magnetic field, which further could be attributed to the rotation of spin-coupled Fe/Cr orbitals under the influence of magnetic field as clear from the magnetic field-dependent Raman spectral analysis. Further, the magnetocapacitance in $PrFe_{1/2}Cr_{1/2}O_3$ ∼5 MHz is found to be 5% at 200 Gauss. The MD coupling percentage has been estimated by using the given formula [3]:

$$MC\ (\%) = \frac{C(H\ T) - C(0\ T)}{C(0\ T)} \times 100. \qquad (5)$$

Here, $C(0\ T)$ and $C(H\ T)$ are the capacitance of material measured at zero and finite magnetic field H Tesla, respectively. Such a large value of magnetocapacitance is noteworthy and could have immense potential applications in data storage devices. This magnetically switchable rotation/retransformation of Fe/Cr orbitals may result in expansion of the material and, hence, may result in an intrinsic MD effect. Therefore, the MD effect can be realized in strongly correlated compounds in terms of contraction/expansion in response to an externally applied magnetic field.

IV. CONCLUSIONS

In summary, the temperature dependence of dielectric, magnetic, and vibrational properties for $PrFe_{1/2}Cr_{1/2}O_3$ was examined in detail using different experimental techniques. The magnetic transition ∼280 K was identified by the magnetic measurements, whereas the anomalies in the unit cell parameters, Raman shift, and dielectric data confirm the presence of strong magnetodielectric and spin-lattice coupling. The origin of natural and external magnetic field induced polar order seems to have a direct relationship with the displacements of Pr atoms and strong SPC, which is jointly corroborated by the global analysis of the results of XRD, INS, and NCS experiments, as well as by the NRTA. The origin of magnetodielectric coupling has been

explained in terms of rotation of spin-coupled Fe orbitals and Pr ion displacement under the influence of the magnetic field, which is corroborated by the magnetic field-dependent Raman spectral analysis. As a final remark, this paper reveals that the intrinsic magnetodielectric effect can be realized in strongly correlated compounds that contract/expand in response to an externally applied magnetic field, and such materials could have immense potential application in data storage devices.

[1] G. Lawes, A. P. Ramirez, C. M. Varma, and M. A. Subramanian, Magnetodielectric Effects from Spin Fluctuations in Isostructural Ferromagnetic and Antiferromagnetic Systems, Phys. Rev. Lett. **91**, 257208 (2003).

[2] T. Kimura, S. Kawamoto, I. Yamada, M. Azuma, M. Takano, and Y. Tokura, Magnetocapacitance effect in multiferroic $BiMnO_3$, Phys. Rev. B **67**, 180401(R) (2003).

[3] M. K. Warshi, A. Kumar, and P. R. Sagdeo, Design and development of a fully automated experimental setup for *in situ* temperature dependent magneto-dielectric measurements, Meas. Sci. Technol. **30**, 125901 (2019).

[4] A. Kumar, M. K. Warshi, M. Gupta, and P. R. Sagdeo, The magneto-elastic and optical properties of multiferroic $GaFeO_{3-\delta}$, J. Magn. Magn. Mater. **514**, 167210 (2020).

[5] S. Manipatruni, D. Nikonov, C.-C. Lin, T. Gosavi, H. Liu, B. Prasad, Y. Lin Huang, E. Bonturim, R. Ramesh, and I. Young, Scalable energy-efficient magnetoelectric spin-orbit logic, Nature **565**, 35 (2019).

[6] N. A. Spaldin, Multiferroics: Past, present, and future, MRS Bull. **42**, 385 (2017).

[7] X. S. Xu, T. V. Brinzari, S. Lee, Y. H. Chu, L. W. Martin, A. Kumar, S. McGill, R. C. Rai, R. Ramesh, V. Gopalan, S. W. Cheong, and J. L. Musfeldt, Optical properties and magnetochromism in multiferroic $BiFeO_3$, Phys. Rev. B **79**, 134425 (2009).

[8] N. A. Hill, Why are there so few magnetic ferroelectrics? J. Phys. Chem. B **104**, 6694 (2000).

[9] A. Sati, A. Kumar, V. Mishra, K. Warshi, P. Pokhriyal, A. Sagdeo, and P. R. Sagdeo, Temperature-dependent dielectric loss in $BaTiO_3$: Competition between tunnelling probability and electron-phonon interaction, Mater. Chem. Phys. **257**, 123792 (2021).

[10] V. S. Bhadram, B. Rajeswaran, A. Sundaresan, and C. Narayana, Spin-phonon coupling in multiferroic $RCrO_3(R = Y, Lu, Gd, Eu, Sm)$: A Raman study, EPL **101**, 17008 (2013).

[11] M. K. Warshi, A. Kumar, V. Mishra, A. Sati, A. Sagdeo, R. Kumar, and P. R. Sagdeo, Effect of self-doping on the charge state of Fe ions and crystal field transitions in $YFeO_3$: Experiments and theory, J. Appl. Phys. **125**, 204101 (2019).

[12] A. Kumar, V. Mishra, M. K. Warshi, A. Sati, A. Sagdeo, R. Kumar, and P. R. Sagdeo, Strain induced disordered phonon modes in Cr doped $PrFeO_3$, J. Phys. Condens. Matter **31**, 275602 (2019).

[13] B. Rajeswaran, P. Mandal, R. Saha, E. Suard, A. Sundaresan, and C. N. R. Rao, Ferroelectricity induced by cations of nonequivalent spins disordered in the weakly ferromagnetic perovskites, $YCr_{1-x}M_xO_3$ (M = Fe or Mn), Chem. Mater. **24**, 3591 (2012).

[14] S. A. Wolf, D. D. Awschalom, R. A. Buhrman, J. M. Daughton, S. von Molnár, M. L. Roukes, A. Y. Chtchelkanova, and D. M. Treger, Spintronics: A spin-based electronics vision for the future, Science **294**, 1488 (2001).

[15] N. D. Tho, D. Van Huong, P. Q. Ngan, G. H. Thai, D. T. A. Thu, D. T. Thu, N. T. M. Tuoi, N. N. Toan, and H. T. Giang, Effect of sintering temperature of mixed potential sensor $Pt/YSZ/LaFeO_3$ on gas sensing performance, Sens. Actuators B Chem. **224**, 747 (2016).

[16] R. Iida, T. Satoh, T. Shimura, K. Kuroda, B. A. Ivanov, Y. Tokunaga, and Y. Tokura, Spectral dependence of photoinduced spin precession in $DyFeO_3$, Phys. Rev. B **84**, 064402 (2011).

[17] Y. S. Didosyan, H. Hauser, G. A. Reider, and W. Toriser, Fast latching type optical switch, J. Appl. Phys. **95**, 7339 (2004).

[18] N. Spaldin, Multiferroics beyond electric-field control of magnetism, Proc. R. Soc. Math. Phys. Eng. Sci. **476**, 20190542 (2020).

[19] U. Chowdhury, S. Goswami, A. Roy, S. Rajput, A. K. Mall, R. Gupta, S. D. Kaushik, V. Siruguri, S. Saravanakumar, S. Israel, R. Saravanan, A. Senyshyn, T. Chatterji, J. F. Scott, A. Garg, and D. Bhattacharya, Origin of ferroelectricity in orthorhombic $LuFeO_3$, Phys. Rev. B **100**, 195116 (2019).

[20] Y. Tokunaga, N. Furukawa, H. Sakai, Y. Taguchi, T. Arima, and Y. Tokura, Composite domain walls in a multiferroic perovskite ferrite, Nat. Mater. **8**, 558 (2009).

[21] Z. J. Huang, Y. Cao, Y. Y. Sun, Y. Y. Xue, and C. W. Chu, Coupling between the ferroelectric and antiferromagnetic orders in $YMnO_3$, Phys. Rev. B **56**, 2623 (1997).

[22] B. Rajeswaran, D. I. Khomskii, A. K. Zvezdin, C. N. R. Rao, and A. Sundaresan, Field-induced polar order at the Néel temperature of chromium in rare-earth orthochromites: Interplay of rare-earth and Cr magnetism, Phys. Rev. B **86**, 214409 (2012).

[23] J.-H. Lee, Y. K. Jeong, J. H. Park, M.-A. Oak, H. M. Jang, J. Y. Son, and J. F. Scott, Spin-Canting-Induced Improper

Ferroelectricity and Spontaneous Magnetization Reversal in $SmFeO_3$, Phys. Rev. Lett. **107**, 117201 (2011).

[24] H. Katsura, N. Nagaosa, and A. V. Balatsky, Spin Current and Magnetoelectric Effect in Noncollinear Magnets, Phys. Rev. Lett. **95**, 057205 (2005).

[25] C. Zhang, M. Shang, M. Liu, T. Zhang, L. Ge, H. Yuan, and S. Feng, Multiferroicity in $SmFeO_3$ synthesized by hydrothermal method, J. Alloys Compd. **665**, 152 (2016).

[26] Y. Yang, H. Xiang, H. Zhao, A. Stroppa, J. Zhang, S. Cao, J. Íñiguez, L. Bellaiche, and W. Ren, Improper ferroelectricity at antiferromagnetic domain walls of perovskite oxides, Phys. Rev. B **96**, 104431 (2017).

[27] K. Dey, A. Indra, S. Mukherjee, S. Majumdar, J. Strempfer, O. Fabelo, E. Mossou, T. Chatterji, and S. Giri, Natural ferroelectric order near ambient temperature in the orthoferrite $HoFeO_3$, Phys. Rev. B **100**, 214432 (2019).

[28] W. Eerenstein, N. D. Mathur, and J. F. Scott, Multiferroic and magnetoelectric materials, Nature **442**, 759 (2006).

[29] F. Pomiro, R. D. Sánchez, G. Cuello, A. Maignan, C. Martin, and R. E. Carbonio, Spin reorientation, magnetization reversal, and negative thermal expansion observed in $RFe_{0.5}Cr_{0.5}O_3$ perovskites ($R =$ Lu, Yb, Tm), Phys. Rev. B **94**, 134402 (2016).

[30] C.-Y. Kuo *et al.*, Komarek, $k = 0$ Magnetic Structure and Absence of Ferroelectricity in $SmFeO_3$, Phys. Rev. Lett. **113**, 217203 (2014).

[31] J. Y. Yang, X. D. Shen, V. Pomjakushin, L. Keller, E. Pomjakushina, Y. W. Long, and M. Kenzelmann, Characterization of magnetic symmetry and electric polarization of $YCr_{0.5}Fe_{0.5}O_3$, Phys. Rev. B **101**, 014415 (2020).

[32] G. Kotnana, V. G. Sathe, and S. N. Jammalamadaka, Spin-phonon coupling in $HoCr_{1-x}Fe_xO_3$ ($x = 0$ and 0.5) compounds, J. Raman Spectrosc. **49**, 764 (2018).

[33] A. Kumar, M. K. Warshi, V. Mishra, A. Sati, S. Banik, A. Sagdeo, R. Kumar, and P. R. Sagdeo, Optical spectroscopy: An effective tool to probe the origin of dielectric loss in Cr doped $PrFeO_3$, Ceram. Int. **45**, 8585 (2019).

[34] A. Kumar, M. K. Warshi, V. Mishra, S. K. Saxena, R. Kumar, and P. R. Sagdeo, Strain control of Urbach energy in Cr-doped $PrFeO_3$, Appl. Phys. A **123**, 576 (2017).

[35] M. K. Warshi, A. Kumar, A. Sati, S. Thota, K. Mukherjee, A. Sagdeo, and P. R. Sagdeo, Cluster glass behavior in orthorhombic $SmFeO_3$ perovskite: Interplay between spin ordering and lattice dynamics, Chem. Mater. **32**, 1250 (2020).

[36] M. Gupta, A. Kumar, A. Sagdeo, and P. R. Sagdeo, Doping-induced combined Fano and phonon confinement effect in La-doped CeO_2: Raman spectroscopy analysis, J. Phys. Chem. C **125**, 2648 (2021).

[37] A. Kumar, S. Umrao, and P. R. Sagdeo, Orbital facilitated charge transfer originated phonon mode in Cr-substituted $PrFeO_3$: A brief Raman study, J. Raman Spectrosc. **51**, 1210 (2020).

[38] A. Kumar, M. K. Warshi, A. Sagdeo, M. Gupta, and P. R. Sagdeo, New route to estimate the Mott-Hubbard and charge transfer parameters: An optical and x-ray absorption studies, Solid State Sci. **115**, 106582 (2021).

[39] V. Mishra, A. Kumar, A. Sagdeo, and P. R. Sagdeo, Comparative structural and optical studies on pellet and powder samples of $BaTiO_3$ near phase transition temperature, Ceram. Int. **46**, 3250 (2020).

[40] See Supplemental Material at http://link.aps.org/supplemental/10.1103/PhysRevB.104.035101 for the arguments in support of this paper in the form of figures and some extra characterization data.

[41] M. Krzystyniak, G. Romanelli, M. Fabian, M. Gutmann, G. Festa, L. Arcidiacono, M. Gigg, K. Drużbicki, C. Andreani, R. Senesi, and F. Fernandez-Alonso, VESUVIO+: The current testbed for a next-generation epithermal neutron spectrometer, J. Phys. Conf. Ser. **1021**, 012026 (2018).

[42] C. Andreani, M. Krzystyniak, G. Romanelli, R. Senesi, and F. Fernandez-Alonso, Electron-volt neutron spectroscopy: Beyond fundamental systems, Adv. Phys. **66**, 1 (2017).

[43] G. Romanelli, M. Krzystyniak, R. Senesi, D. Raspino, J. Boxall, D. Pooley, S. Moorby, E. Schooneveld, N. J. Rhodes, C. Andreani, and F. Fernandez-Alonso, Characterisation of the incident beam and current diffraction capabilities on the VESU-VIO spectrometer, Meas. Sci. Technol. **28**, 095501 (2017).

[44] M. Krzystyniak, K. Drużbicki, S. Rudić, and M. Fabian, Positional, isotopic mass and force constant disorder in molybdate glasses and their parent metal oxides as observed by neutron diffraction and Compton scattering, J. Phys. Commun. **4**, 095027 (2020).

[45] R. Haworth, J. L. Shaw, A. C. Wright, R. N. Sinclair, K. S. Knight, J. W. Taylor, N. Vedishcheva, I. Polyakova, B. A. Shakhmatkin, S. A. Feller, and D. Winslow, Superstructural units in vitreous and crystalline cæsium borates, Phys. Chem. Glas. **46**, 477 (2005).

[46] S. F. Parker, F. Fernandez-Alonso, A. J. Ramirez-Cuesta, J. Tomkinson, S. Rudic, R. S. Pinna, G. Gorini, and J. Fernández Castañon, Recent and future developments on TOSCA at ISIS, J. Phys. Conf. Ser. **554**, 012003 (2014).

[47] D. Colognesi, M. Celli, F. Cilloco, R. Newport, S. F. Parker, V. Rossi-Albertini, F. Sacchetti, J. Tomkinson, and M. Zoppi, TOSCA neutron spectrometer: The final configuration, Appl. Phys. A **74**, s64 (2002).

[48] Z. A. Bowden, M. Celli, F. Cilloco, D. Colognesi, R. J. Newport, S. F. Parker, F. P. Ricci, V. Rossi-Albertini, F. Sacchetti, J. Tomkinson, and M. Zoppi, The TOSCA incoherent inelastic neutron spectrometer: Progress and results, Physica B Condens. Matter **276-278**, 98 (2000).

[49] S. F. Parker, C. J. Carlile, T. Pike, J. Tomkinson, R. J. Newport, C. Andreani, F. P. Ricci, F. Sacchetti, and M. Zoppi, TOSCA: A world class inelastic neutron spectrometer, Physica B Condens. Matter **241–243**, 154 (1997).

[50] R. Pinna, S. Rudić, S. Parker, J. Armstrong, M. Zanetti, G. Škoro, S. Waller, D. Zacek, C. Smith, M. Capstick, D. McPhail, D. Pooley, G. Howells, G. Gorini, and F. Fernandez-Alonso, The neutron guide upgrade of the TOSCA spectrometer, Nucl. Instrum. Methods Phys. Res. **896**, 68 (2018).

[51] B. S. Hudson, Vibrational spectroscopy using inelastic neutron scattering: Overview and outlook, Vib. Spectrosc. **42**, 25 (2006).

[52] A. Kumar, O. V. Rambadey, and P. R. Sagdeo, Unorthodox approach to realize the correlation between the dielectric constant and electronic disorder in Cr-doped $PrFeO_3$, J. Phys. Chem. C **125**, 7378 (2021).

[53] N. K. C. Muniraju, *Crystal and Spin Structure and Their Relation to Physical Properties in Some Geometrical and Spin Spiral Multiferroics* (Forschungszentrum Jülich, Jülich, 2012).

[54] A. Sati, P. Pokhriyal, A. Kumar, S. Anwar, A. Sagdeo, N. P. Lalla, and P. R. Sagdeo, Origin of ferroelectricity in cubic phase of Hf substituted $BaTiO_3$, J. Phys. Condens. Matter **33**, 165403 (2021).

[55] L. H. Yin, J. Yang, R. R. Zhang, J. M. Dai, W. H. Song, and Y. P. Sun, Multiferroicity and magnetoelectric coupling enhanced large magnetocaloric effect in $DyFe_{0.5}Cr_{0.5}O^3$, Appl. Phys. Lett. **104**, 032904 (2014).

[56] J. B. Goodenough, Theory of the role of covalence in the perovskite-type manganites [La, M(II)]MnO_3, Phys. Rev. **100**, 564 (1955).

[57] J. B. Goodenough and A. L. Loeb, Theory of ionic ordering, crystal distortion, and magnetic exchange due to covalent forces in spinels, Phys. Rev. **98**, 391 (1955).

[58] T. Hashimoto, Magnetic properties of the solid solutions between $KMnF_3$, $KCoF_3$ and $KNiF_3$, J. Phys. Soc. Jpn. **18**, 1140 (1963).

[59] J. C. Walling and R. L. White, Study of magnetic interactions in $HoFeO_3$, Phys. Rev. B **10**, 4748 (1974).

[60] W. C. Koehler, E. O. Wollan, and M. K. Wilkinson, Neutron diffraction study of the magnetic properties of rare-earth-iron perovskites, Phys. Rev. **118**, 58 (1960).

[61] A. Sati, V. Mishra, A. Kumar, M. K. Warshi, A. Sagdeo, R. Kumar, and P. R. Sagdeo, Effect of structural disorder on the electronic and phononic properties of Hf doped $BaTiO_3$, J. Mater. Sci. Mater. Electron. **30**, 9498 (2019).

[62] E. Granado, A. García, J. A. Sanjurjo, C. Rettori, I. Torriani, F. Prado, R. D. Sánchez, A. Caneiro, and S. B. Oseroff, Magnetic ordering effects in the Raman spectra of $La_{1-x}Mn_{1-x}O_3$, Phys. Rev. B **60**, 11879 (1999).

[63] M. Balkanski, R. F. Wallis, and E. Haro, Anharmonic effects in light scattering due to optical phonons in silicon, Phys. Rev. B **28**, 1928 (1983).

[64] A. Kumar, A. Sati, V. Mishra, M. K. Warshi, R. Kumar, and P. R. Sagdeo, Charge neutral crystal field transitions: A measure of electron-phonon interaction, J. Phys. Chem. Solids **135**, 109102 (2019).

[65] M. Fiebig, T. Lottermoser, D. Meier, and M. Trassin, The evolution of multiferroics, Nat. Rev. Mater. **1**, 16046 (2016).

[66] H. J. Zhao, L. Bellaiche, X. M. Chen, and J. Íñiguez, Improper electric polarization in simple perovskite oxides with two magnetic sublattices, Nat. Commun. **8**, 14025 (2017).

[67] B. B. Van Aken, T. T. M. Palstra, A. Filippetti, and N. A. Spaldin, The origin of ferroelectricity in magnetoelectric $YMnO_3$, Nat. Mater. **3**, 164 (2004).

[68] Z. Li, Y. Wang, Y. Lin, and C. Nan, Evidence for stress-mediated magnetoelectric coupling in multiferroic bilayer films from magnetic-field-dependent Raman scattering, Phys. Rev. B **79**, 180406(R) (2009).

[69] G. Burns and B. A. Scott, Lattice modes in ferroelectric perovskites: $PbTiO_3$, Phys. Rev. B **7**, 3088 (1973).

[70] D. Colognesi, C. Andreani, and E. Degiorgi, Phonon density of states from a crystal-analyzer inverse-geometry spectrometer: A study on ordered solid hydrogen sulfide and hydrogen chloride, J. Neutron Res. **11**, 123 (2003).

[71] M. B. Chadwick *et al.*, ENDF/B-VII.0: Next generation evaluated nuclear data library for nuclear science and technology, Nucl. Data Sheets **107**, 2931 (2006).

[72] Z. H. Sun, B. L. Cheng, S. Dai, L. Z. Cao, Y. L. Zhou, K. J. Jin, Z. H. Chen, and G. Z. Yang, Dielectric property studies of multiferroic $GaFeO_3$, J. Phys. Appl. Phys. **39**, 2481 (2006).